Application of Fe-doped SnO$_2$ nanoparticles in organic solar cells with enhanced stability

M.S. Pereira [a, *], F.A.S. Lima [a, b], T.S. Ribeiro [a], M.R. da Silva [c], R.Q. Almeida [d], E.B. Barros [d], I.F. Vasconcelos [a]

[a] Department of Metallurgical and Material Engineering, Universidade Federal do Ceará, Fortaleza, Brazil
[b] Org. Electron. Division, CSEM Brasil, Belo Horizonte, Brazil
[c] Institute of Physics and Chemistry, Universidade Federal de Itajubá, Itajubá, Brazil
[d] Department of Physics, Universidade Federal do Ceará, Fortaleza, Brazil

ABSTRACT

Solution-processed P3HT:PCBM-based bulk heterojunction organic solar cells were constructed with Fe-doped tin oxide (Fe/SnO$_2$) magnetic nanoparticles (NP) incorporated to the active layer. Performance and stability of devices were evaluated. Devices reinforced with Fe/SnO$_2$ nanoparticles showed improvement in short-circuit current density J$_{sc}$ up to 10%, when compared with devices without the addition of NPs. Improved J$_{sc}$ was attributed to the extension of photogenerated exciton lifetime as a result of the magnetic field provided by the NPs. Life time and stability tests revealed extended T$_{80}$ for samples reinforced with NPs for both indoor and outdoor tests, which can be attributed to slightly improvements of fill factor during aging tests. Moreover, NP-reinforced devices have shown the tendency to overcome the burn-in regime faster. These results are indications that the addition of diluted magnetic semi-conductor oxide nanoparticles in the active layer of organic solar cells has the potential to contributed to the extension of lifetime and improvement of stability of these devices.

© 2017 Elsevier B.V. All rights reserved.

1. Introduction

Organic solar cells (OSCs) are showing rapid advances in efficiency and potential for technological applications. In recent years, bulk heterojunction (BHJ) OSCs have attracted attention for both academic and industrial sectors due to their premium features of flexibility, fabrication simplicity, low manufacturing costs, short energy payback time, and low environmental impact [1–3]. In 2016, the companies Raynergy Tek and Heliatek reported power conversion efficiencies (PCE) over 11% for single junction cells and as high as 13% for tandem small molecule cells, respectively. This indicates that OSCs are strongly competitive against their inorganic counterparts [4]. As the most reported architecture of OSCs, the BHJ structure comprises an interpenetrating network of a conjugated polymer donor such as poly(3-hexylthiophene-2,5-diyl) (P3HT) and a soluble fullerene acceptor which is typically [6,6]-phenyl-C$_{60}$-butyric acid methyl ester (PCBM) as the photoactive layer [5–9]. P3HT:PCBM BHJ OSCs was one of the first studied OSCs and

still is the most widely studied structure, as both P3HT and PCBM materials are commercially available and more affordable.

Most recent studies on P3HT:PCBM BHJ-OSCs have been focused on optimizing microphase separation by choosing proper solvents for processing the photoactive layers [8,10–12] or by post-thermal treatment of the photoactive layers [8,10,13]. Given the difficulty to tune the morphology between donor and acceptor materials at such small scales, another way around this issue that has gained attention consists of increasing the effective lifetime of the photogenerated excitons, and thereby their diffusion length [14–16].

It is known that in organic materials such as P3HT the primary photo-generated charge carriers are Coulomb-bound electronhole pairs, so-called excitons, which lie in both singlet states and triplet states with different lifetimes. Only the dissociated excitons, i.e., Coulomb-bound electronhole pairs dissociated into free charge carriers, could contribute to the photocurrent. One major bottleneck for the efficiency of this process is that in P3HT the singlet lifetime is approximately 300 ps and the resulting singlet exciton diffusion length is reported in the range of 3–6 nm [14,17,18]. In contrast, the P3HT triplet lifetime is in the order of 10 μs implying a triplet exciton diffusion length of the order of 100 nm [19], which

aids their diffusion process toward donor-acceptor junctions and thus enhances the photovoltaic process in OSCs [14]. The migration of excitonic states from the excited singlet to the triplet can occur in the presence of strong spinorbit coupling. This transition is known as intersystem crossing.

Magnetic nanoparticles, ferromagnetic domain boundaries, and surfaces exhibiting antiferromagnetism are amongst nano-structures that may bring about current enhancement [20]. Several recent observations suggest that magnetic nanostructures may induce unusual spin dynamics of electrons in nearby organic molecules. These effects include enhanced quantum efficiency, magnetically modulated quantum efficiency [21] in organic LEDs doped with magnetic nanoparticles. Recently, several groups of researchers have reported improvements in efficiency and stability with insertion of NPs in BHJ CSOs [5–7,22,23].

Despite considerable improvement of OSCs PCE values, their poor stability and short carriers lifetime are still issues that need to be addressed before this technology becomes commercially viable. Organic solar cells degrade due to a number of factors, such as exposure to high temperatures and UV-light, water or oxygen intake, mechanical stress, among others [24–26]. One of the stra-tegies that have been applied to improve OSCs lifetime and stability is the replacement of highly hygroscopic [27,28] PEDOT:PSS as hole transport material (HTL). Over the last few years, transition metal oxides with large work function like NiO [29], MoO_3 [30,31], WO_3 [32] and V_2O_5 [33,34] among others, have been shown to be viable options as hole-transport layer in stable OSCs. In fact, water-based V_2O_5 was found be highly compatible with printing techniques [35] and was used as HTL for all OSCs used in this work.

In this paper, we introduce Fe doped SnO_2 (Fe/SnO_2) magnetic nanoparticles (NPs) into P3HT:PCBM BHJ OSCs and find that the doping of NPs result in the enhancement of the J_{sc} and stability. In order to discuss in which way the performance of OSCs doped with NPs is mainly affected, we present a study based on the model system P3HT:PCBM solar cells blended with weight concentration of 10% NPs.

2. Experimental procedure

2.1. Synthesis of Fe/SnO₂ nanoparticles

Fe/SnO$_2$ nanoparticle (Fe:Sn molar ratio of 1:10) samples were prepared by high-energy ball milling. Commercial SnO_2 and Fe_2O_3 (Sigma-Aldrich, 99.9%) powders together with alumina vials and zirconia spheres (ball-to-powder mass ratio of 20:1) were used in a planetary mill (Fritsch Pulverissette 6) operating with an angular velocity of 500 rpm.

2.2. Solar cell fabrication

Two types of solar cell devices were prepared with inverted configuration and tested in air under ambient conditions: reference devices (ref-OSC) with configuration FTO/ZnO/P3HT:PCBM/V_2O_5/Ag; and nanoparticle-bearing devices (NP-OSC) with configuration FTO/ZnO/P3HT:NP:PCBM/V_2O_5/Ag.

A 30 nm thick electron transport layer (ETL) was deposited from a solution of ZnO in chlorobenzene (40 mg/ml) that was spin-coated at 3000 rpm on the FTO surface and dried at 140° C for 30 min at air atmosphere conditions. This solution was produced by collaborators [8].

The bulk heterojunction blend of ref-OSCs comprised of a 1:1 M mixture of P3HT:PCBM dissolved in 1,2-dichlorobenzene while that of NP-OSCs comprised of a molar 0.9:0.1:1 mixture of P3HT:NP:PCBM. The nanoparticles were suspended in 1,2-dichlorobenzene (30 mg/ml) and mixed added to the P3HT:PCBM blend to achieve the desired concentration. Blends were spin coated at 1000 rpm to deposit a 300 nm-thick P3HT:PCBM and P3HT:NP:PCBM films.

A 120-nm thick hole transport layer (HTL) was deposited from a molar 1:1 solution of V_2O_5 sol-gel:isopropanol that was spin-coated at 3000 rpm and annealed at 120° C for 1–2 min on a hot plate at atmosphere conditions. The V_2O_5 sol-gel was produced by collaborators [8].

Finally, a 100 nm-thick Ag back metal electrode was deposited by thermal evaporation in an evaporation system (Auto 306, BOC Edwards). The devices were subsequently annealed at 120° C for 10 min in air. A set of six ref-OSC and NP-OSC devices were pre-pared for the tests of efficiency and stability.

2.3. Characterization

X-ray diffraction (XRD) patterns of powdered nanoparticles were collected at room temperature using a Rigaku DMAXB diffractometer operating with a Kα-Cu source ($\lambda = 1.54$ Å) at 40 kV and 30 mA. The data were collected in a range of $20°-100°$ in 2θ and the pattens were Rietveld refined using the program GSAS [36].

Magnetization measurements of powdered nanoparticles were carried out at room temperature using a Lakeshore (model 7404) vibrating sample magnetometer (VSM) with maximum field of 27 kOe. Room temperature Mössbauer spectra were measured in transmission mode using a ^{57}Co(Rh) radioactive source mounted on a velocity driver operating in sinusoidal mode. The data were evaluated by least square fitting to series of discrete Lorentzian shaped subspectra by means of the software package Normos. Isomer shifts (δ) are quoted with respect to α-Fe.

Active layer film samples for atomic force microscopy (AFM), conductive atomic force microscopy (c-AFM) and scanning electron microscopy (SEM) were prepared via spin-coating of blends on a glass substrate covered with a 30 nm layer of ZnO. AFM and c-AFM measurements were done in air under ambient conditions using an Asylum Research scanning probe microscope. Images were collected in tapping mode using a Nanoworld (model Arrow CONTPt) Pt-coated Si probe with a spring constant of 0.2 N/m. SEM measurements were performed in air under ambient conditions using a Quanta FEG 450 microscope.

Solar simulations was performed on a KHS1200 (Steuernagel Solarkonstant) equipped with an AM1.5 filter (100 mW/cm^2, AM1.5G, 72° C). J × V curves were measured using a Keithley 2601 multimeter with light intensity of 100 mW, calibrated with a Zipp & Konen CM-4 pyranometer, which was used constantly during measurements to set light intensity. A calibrated S1227-1010BQ photodiode from Hamamatsu was also applied for calibration before each measurement. Incident photon-to-electron conversion efficiency (IPCE) analyses were done with a QE/IPCE measurement System from Oriel (from 300 to 800 nm; at 10 nm intervals). The results were not corrected for any intensity losses due to light ab-sorption or reflection by the glass support.

3. Results and discussion

3.1. Fe/SnO₂ nanoparticles

Fig. 1 shows the XRD pattern of a Fe/SnO$_2$ nanoparticle sample. The diffraction peaks correspond to the rutile-type tetragonal structure of SnO_2. No Fe-bearing phase was found indicating total incorporation of Fe_2O_3 by the SnO_2 matrix. The average particle size calculated using Scherrer's equation and corrected by the Williamson-Hall relation (which separates contributions of particle size and residual microstrain to the breadth of diffraction peaks) is about 10 nm.
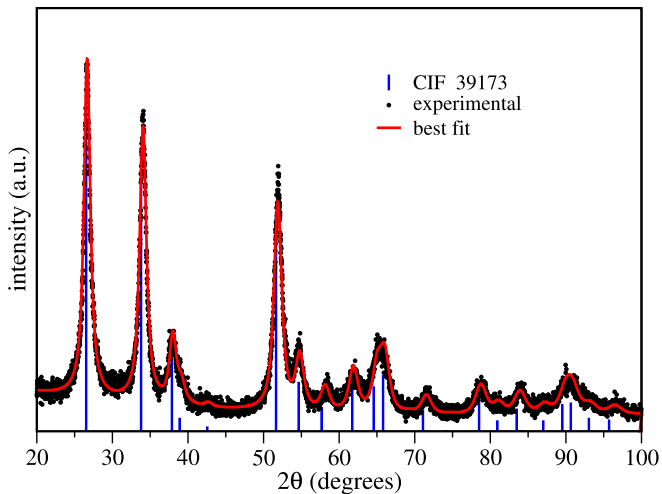
Fig. 1. X-ray diffraction pattern of a Fe/SnO_2 nanoparticle sample. Dots and solid lines are the experimental data and best fit respectively. Bars represent the ICSD-39173 standard pattern.
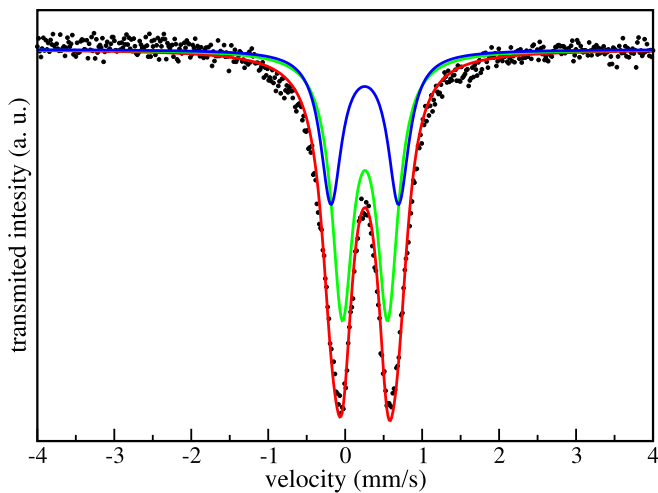

Fig. 2. Mössbauer spectrum of a Fe/SnO_2 nanoparticle sample.

Mössbauer spectra of Fe/SnO_2 nanoparticle sample and respective best fits (achieved using two paramagnetic doublets) are shown in Fig. 2. The absence of sextets confirms the successful incorporation of Fe^{3+} to the matrix. Isomer shift and quadrupole splitting values of both doublets are consistent with octahedral coordinated Fe^{+3} substituting for Sn^{4+} in the SnO_2 [37] matrix.

Fig. 3 shows the magnetization *vs* applied field curve obtained at room temperature from a Fe/SnO_2 nanoparticle sample. The curve consists of a linear paramagnetic component and a magnetic hysteresis loop with coercivity of 145 Oe and remanent magnetization of 6.3×10^{-3} emu/g. These values indicate that the sample is ferromagnetic at room temperature.

3.2. Films morphology

Fig. 4 shows SEM images of (a) ref-OSC and (b) NP-OSC active layer films. The images show PCBM domains (lighter regions) randomly distributed within the P3HT matrix (dark background) [5,38]. The NP-OSC film also show bright spots attributed to clusters of NPs according to energy dispersive X-ray spectrometry results.

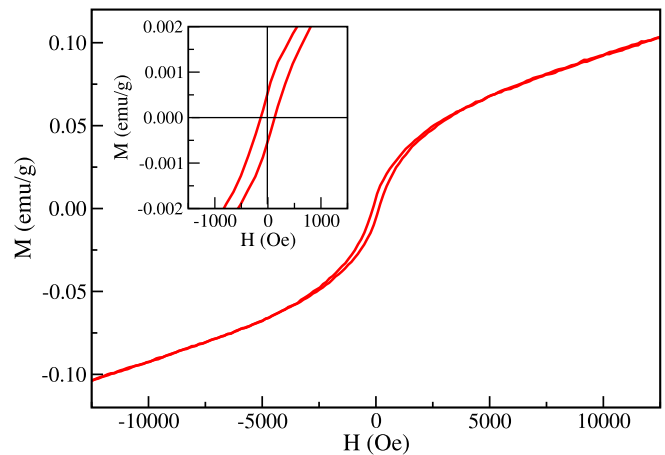Fig. 5 shows AFM and c-AFM images of the active layer of a ref-

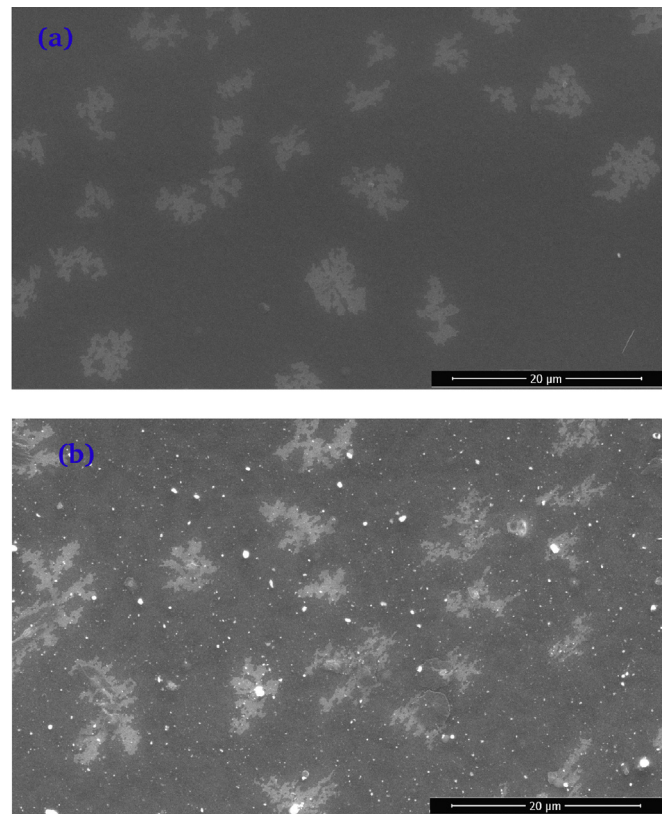**Fig. 3.** Room temperature hysteresis loop of a Fe/SnO_2 nanoparticle sample.

Fig. 4. SEM images of (a) ref-OSC and (b) NP-OSC films.

OSC and a NP-OSC film. In can be observed on the AFM surface topography images – parts (a) and (c) – that the addition of nanoparticles affects the morphology of the film, introducing aggregated domains (bright spots in Fig. 5c) reinforcing the SEM results. Doping induces the formation of NPs clusters that yield uneven film morphology which can lead to decrease of the shunt resistance R_{sh} and consequent increased leakage current [22].

Current AFM images – parts (b) and (d) – was used to examine conductivity variations in the P3HT:NP:PCBM blends. A high work function Pt-coated Si probe was used in all measurements. The high electron injection barrier between the Pt-coated Si tip and the P3HT:NP:PCBM blend blocks electron injection which allows hole
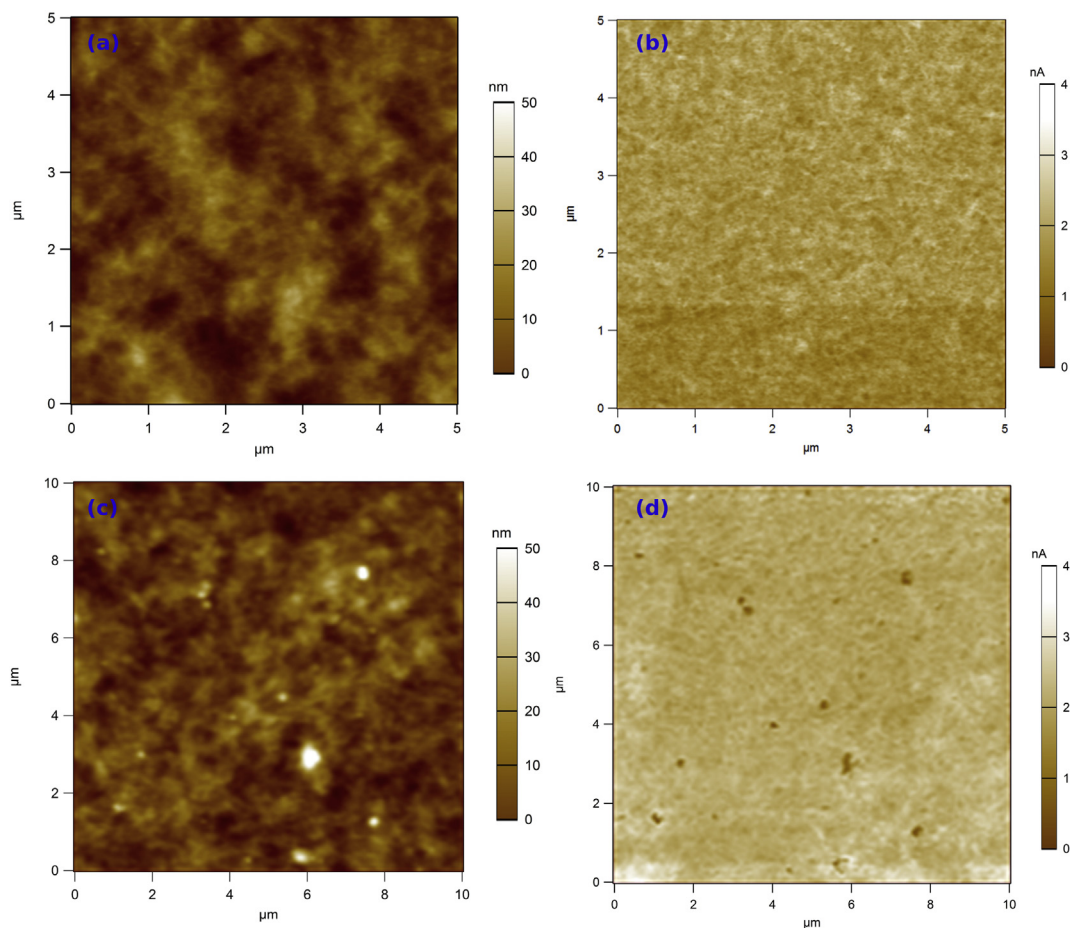
Fig. 5. (a) AFM and (b) c-AFM images of a ref-OSC film; (c) AFM and (d) c-AFM images of a NP-OSC film.

transport only within P3HT [13]. Therefore, bright and dark regions are attributed to P3HT-rich and PCBM-rich domains, respectively. Images of NP-bearing samples show non-conductive dark spots associated to clusters of NPs in the active layer, as was pointed out above.

3.3. Solar cells performance

Fig. 6 shows (a) characteristic $J \times V$ curves (under AM1.5G illumination with light intensity of 100 mW/cm^2) and (b) normalized IPCE spectra of the ref-OSC and NP-OSC cells with the best performance. Photovoltaic parameters for a hero device and the average of the set of six samples of either ref-OSC or NP-OSC type are summarized in Table 1. It can be seen that the photovoltaic parameters of the best cells were very close to the average values of each set of six devices, ensuring good reproducibility of the results.

The devices reinforced with nanoparticles showed a slightly improved J_{sc} with average value increasing from 11.25 to 12.09 mA/cm^2. This suggests that the addition of NPs contributes to the dissociation of photogenerated excitons into free charge carriers resulting in an enlarged short-circuit current density. The broader IPCE spectrum found for NP-OSCs seen in Fig. 6b reinforces this suggestion.

Average V_{oc} was slightly lower for NP-OSCs, which can be attributed to added disorder to the system due to the presence of magnetic nanoparticles [39,40]. Average FF was also lower for NP-OSC. This effect is very often observed in devices with enhanced J_{sc} [41]. The increase in the density of free photogenerated carriers

improves both J_{sc} values and recombination rates due to a competition between recombination and extraction of free charges [41]. The combination of these effects tends to lower FF values.

Series resistance (R_s) and shunt resistance (R_{sh}) were calculated from the slope of $J \times V$ curves and are also shown in Table 1. The increasing on average R_s values for NP-OSC devices is remarkable and most likely due to the presence of NP aggregates as seen on microscopy images.

As mentioned previously, addition of NPs to the active layer of OSCs produced a broader IPCE spectrum (see Fig. 6b). This improvement is observed in the region of longer wavelengths, suggesting that doping has caused a reduction in energy levels HOMO and LUMO of the donor.

3.4. The role of magnetic NPs

Fig. 7 shows measurements of photocurrent density J_{ph} as a function of effective bias voltage (V_0-V). In both cells, photocurrent values increase sharply from zero to about 0.6 V when they slow down gradually as saturation is approached. The slope of the rise is steeper (see inset) and saturation is reached earlier for the reference device. The slightly larger saturation current in NP-OSC devices is attributed to a higher dissociation of photogenerated excitons into free charge carriers. Therefore, the presence of magnetic NPs does not contribute to exciton generation but with the enhancement of excitons dissociation rate.

Due to their ferromagnetism at room temperature, Fe/SnO$_2$ NPs generate a weak effective magnetic field within the OSC
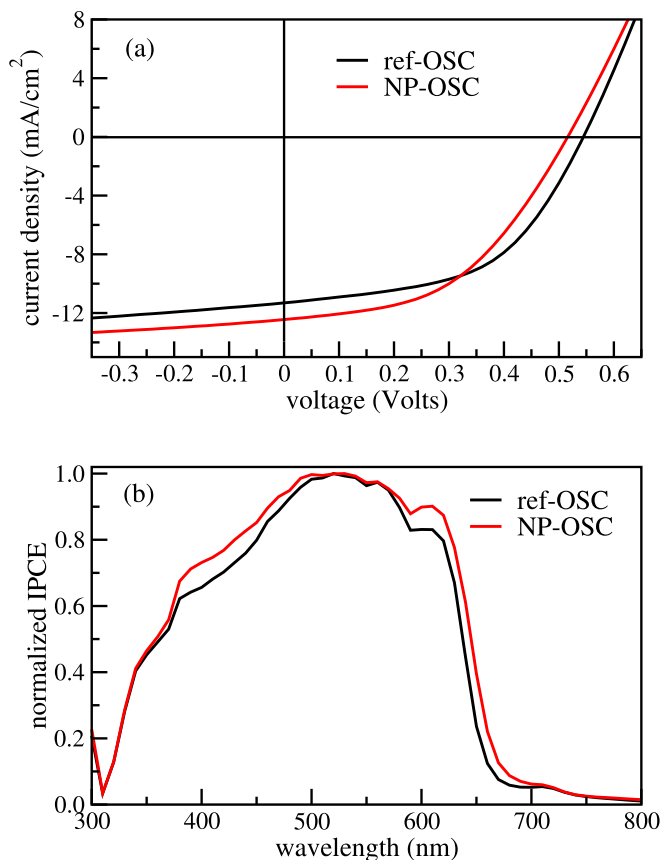
Fig. 6. (a) $J \times V$ curves and (b) normalized IPCE spectra of the best ref-OSC and NP-OSC cells.

crossing. On the other hand, the clustering of NPs enables alternative conducting paths for charge carriers inducing leakage currents. Increasing doping to 0.9:0.1:1 yields a larger magnetic field within the active larger leading to a larger rate of intersystem crossing that overcomes the effect of leakage currents. This suggests that the improvement in J_{sc} values is likely associated with an effective magnetic field generated by the presence of magnetic NPs.

Progress in organic solar cells relies strongly on two features: dissociation of photogenerated excitons into free carriers, and ultrafast electron-hole (e-h) charge separation [42,43]. Evidently understanding the underlying mechanism is useful for the future rational design of new OSCs with improved efficiency and stability, but unfortunately these phenomena cannot be explained completely by the traditional theories. Classical approaches consider the dependence of exciton dissociation on an increasing electric field in the device, as a coulombically bound e-h pair requires a certain electric field for complete separation [44,45]. More sophisticated models incorporate explicitly the delocalization of the photogenerated charges by considering their effective masses [42]. Similarly, electron-phonon coupling [43] can strongly influence the process of exciton diffusion and dissociation dynamics in OSCs.

The exciton binding energy in a typical organic semiconductor has two components: the Coulomb energy of the e-h pair and the additional binding energy of the electron-phonon interaction. For the case that the exciton has negligible electron-phonon coupling, the optical absorption edge is coincident with the exciton energy (assuming a direct gap semiconductor), irrespective of the magnitude of the exciton binding energy. However, when the exciton has strong electron-phonon coupling, the optical absorption is no longer coincident with the exciton energy [43,46]. The AFM and SEM images show a large degree of local disorder introduced by the incorporation of NPs. This disorder causes significant variations in the donor-acceptor interface and, consequently, can influence the dissociation and collection of photogenerated excitons. Due to the disorder caused by the incorporation of NPs, it is possible that the NP-OSC devices have a strong electron-phonon coupling. Therefore, a more complete interpretation requires that the electron-phonon coupling energy must be taken into account.

Arkhipov et al. [47,48] proposes that heavier carriers have smaller energy of zero-point oscillations and such carriers are localized within on-chain potential wells. Therefore, the field-controlled height of on-chain barriers essentially determines the probability of full dissociation and the field dependence of the free carrier yield becomes stronger with increasing effective mass m_{eff}. The effective mass of holes in P3HT is about $1.8m_e$ and is similar to many inorganic semiconductors [49] such as SnO_2 with $m_{eff} \approx 1.6m_e$ [50,51]. Thus, no significant contributions are expected related to the hole effective mass in the NPs.

3.5. Lifetime and stability studies

Organic solar cells degrade due to a number of factors such as light exposure [52,53], high temperatures [54,55], low resistance to

photoactive layer. The effect of magnetic fields on organic solar cells has been studied for different OSCs [6,7,22]. It has been observed that a low magnetic field can increase the rate of intersystem crossing thus increasing the concentration of triplet excitons. The increase of triplet excitons can lead to an increase of dissociated charge carriers due to triplets' longer lifetime in bulk materials as compared to that of singlet excitons, yielding larger currents through the devices [14,22].

In order to clarify the effect of NPs on the enhancement of J_{sc} values, cells with P3HT:NP:PCBM molar ratios of 0:1:1 and 0.95:0.05:1 were fabricated and tested. The 0:1:1 cell exhibited very low J_{sc} (~0.14 mA/cm^2) and PCE (~0.006%) values indicating that these NPs are not an efficient light absorbing material and electron donor.

Devices with 0.95:0.05:1 ratios exhibited smaller J_{sc} values (~9.47 mA/cm^2) than those of the reference devices. This decrease may be associated to the weak magnetism of these NPs. In low concentrations, the magnetic field generated within the active layer is not strong enough to yield a considerable rate of intersystem

Table 1
Photovoltaic parameters and resistance values of ref-OSC and NP-OSC devices.

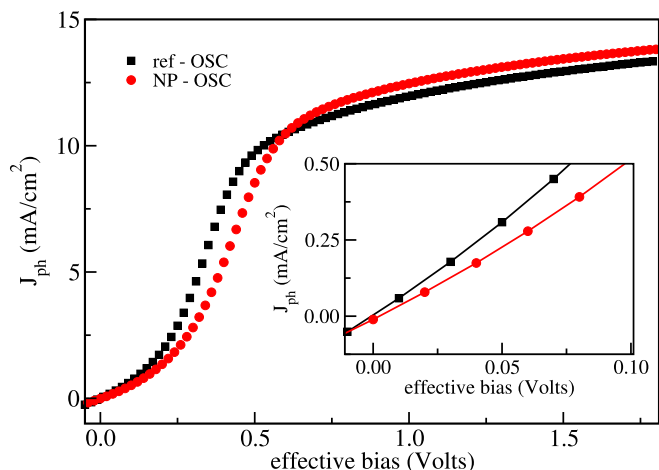| Device	J_{sc} (mA/cm^2)	V_{oc} (V)	FF (%)	η (%)	R_s (Ω cm^2)	R_{sh} (Ω cm^2)
ref-OSC						
Hero	11.30	0.54	52.0	3.20	425	275
Avg	11.25 ± 0.04	0.54 ± 0.0	50.4 ± 1.0	3.06 ± 0.09	553 ± 100	298 ± 17
NP-OSC						
Hero	12.44	0.52	47.34	3.04	1200	411
Avg	12.09 ± 0.24	0.52 ± 0.0	47.24 ± 0.6	2.96 ± 0.06	831 ± 273	321 ± 69

Fig. 7. Plots of photocurrent density with respect to effective bias.

Table 2
ISOS protocols used in this study for lifetime testing of OSCs.

Testing ID	Testing conditions			
	Light source	Temperature	Humidity	Environment
ISOS-L-1	Simulated (1 Sun)	Ambient	Ambient	Light only
ISOS-O-2	Sun light	Ambient	Ambient	Ambient

water and oxygen [56], as well as combinations of these factors and others [57]. In this work, lifetime and stability of OSCs with and without the addition of Fe/SnO_2 nanoparticles were measured according to ISOS standards [58] ISOS-L-1 and ISOS-O-2, outlined in Table 2.

3.5.1. ISOS-L-1 test

ISOS-L-1 tests were performed for 70 h on encapsulated ref-OSC and NP-OSC samples according to the conditions described on Table 2. The time evolution of photovoltaic parameters normalized to their pre-test values is shown in Fig. 8. Relative conversion efficiency η for both devices is shown in part (a). It can observed that the NP-bearing device presented a slightly better stability, reaching T_{80} after 40 h while the sample without NPs reached T_{80} after about 15 h.

Fig. 8b and c shows the time evolution of relative photovoltaic parameters of ref-OSC and NP-OSC devices, respectively. V_{oc} of both devices remains relatively unchanged during the test, suggesting that the chemical potential and charge transfer energy across the devices did not change significantly.

Values of J_{sc} for both devices follow the time evolution recorded for conversion efficiency, with a steeper drop during the first few hours before reaching a plateau. The time consumed during this initial strong drop is referred to as burn-in time [59], which is a signature of light induced degradation [60–63]. Many factors can be responsible to this burn-in process. Polymer conjugation losses (e. g. chemical degradation of the electron donor in the active layer), decrease of donor/acceptor interface area due to increase of blend domains above the diffusion length of the exciton, and ordering of the polymer chains (e.g. due to chain scission) all contribute to cell degradation as they affect charge transport [64].

As J_{sc} tends to stabilize after some hours, the dominant degradation mechanism is expected to saturate. Street et al. [65] and Bhattacharya et al. [66] have described analogous drops on J_{sc} due to the creation of mid-gap defect states at the donor/acceptor
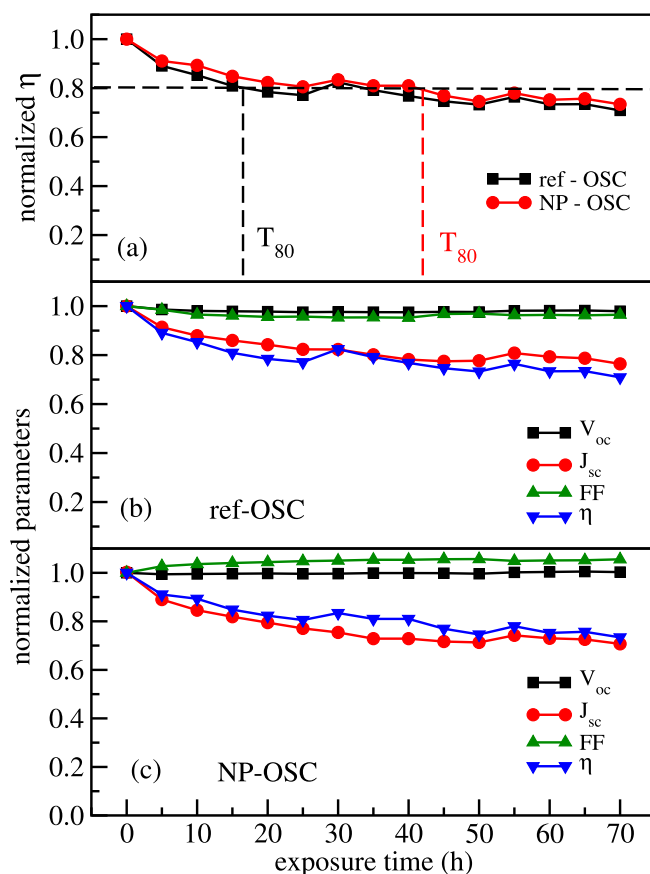

Fig. 8. ISOS-L-1 test: (a) time evolution of conversion efficiency η of ref-OSC and NP-OSC; (b) time evolution of ref-OSC photovoltaic parameters; and (c) time evolution of NP-OSC photovoltaic parameters. All quantities normalized to their pre-test values.

interface due to prolonged light exposure. Several groups [67–70] described the same behavior attributing this lowering on J_{sc} to fullerene dimerization.

Fill factor values remain almost constant during the test with a slight increase recorded for the NP-OSC device. This improvement in FF for NP-OSC can be an indication that the addition of Fe/SnO_2 nanoparticles turned the device less sensitive to light soaking [71,72]. The slight increase in FF with time together with the higher initial J_{sc} for the NP-OSC makes the addition of Fe/SnO_2 nanoparticles on the active layer a promising approach to improve the lifetime of OSCs.

Fig. 9 shows a comparison of ref-OSC and NP-OSC normalized IPCE spectra before and after the ISOS-L-1 test. IPCE losses are clear in the 350–450 nm and 550–650 mn ranges and more pronounced for the NP-OSC device. Absorption in the range of 350–450 nm is mostly due to fullerene domains, which is an indication that the fullerene dimerization process was more intense in the NP-bearing OSC. As fullerene does not absorb light in the 550–650 mn range, these losses must be related with P3HT degradation or oxide opacity in this range.

3.5.2. ISOS-O-2 test

To further evaluate the stability of NP-bearing solar cells, ISOS-O-2 standard tests under realistic conditions described on Table 2 were performed. Encapsulated ref-OSC and NP-OSC samples were attached to a solar tracker system and placed on the roof of the Catalan Institute of Nanoscience and Nanotechnology in Barcelona, Spain (41° 30′ 8″ latitude and 2° 6′ 42″ longitude) for 21 days. The
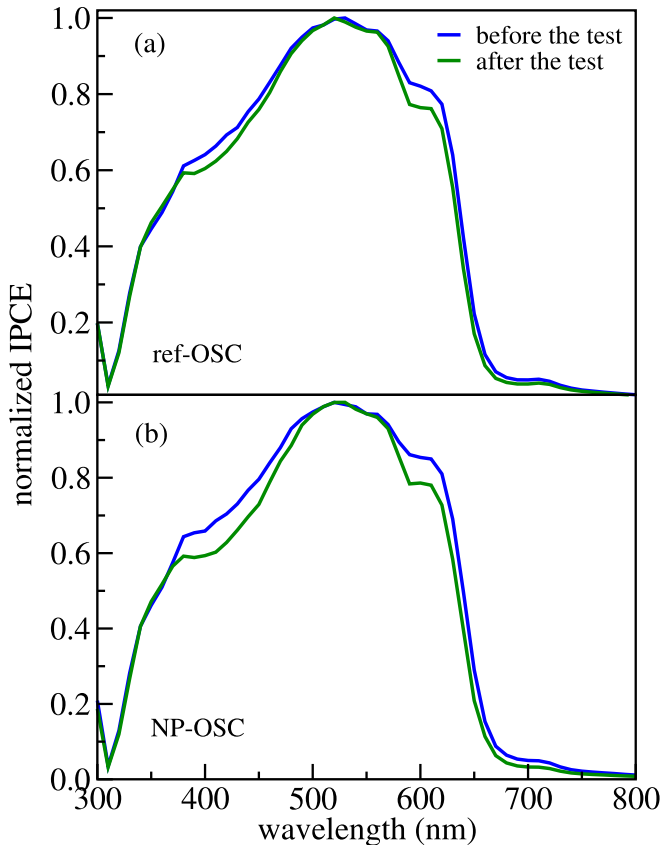
Fig. 9. ISOS-L-1 test: normalized IPCE measurements before and after the test for (a) ref-OSC and (b) NP-OSC devices.

Fig. 10. ISOS-O-2 test: (a) time evolution of conversion efficiency η of ref-OSC and NP-OSC; (b) time evolution of ref-OSC photovoltaic parameters; and (c) time evolution of NP-OSC photovoltaic parameters. All quantities normalized to their pre-test values.

cells were characterized periodically by means of $J \times V$ measurements under real solar illumination.

Time evolution of conversion efficiency η for both samples is singled out in Fig. 10a while time evolution of V_{oc}, J_{sc}, η and FF is shown in Fig. 10b (ref-OSC) and Fig. 10c (NP-OSC). All parameters were normalized to their pre-test values. The data showed that samples in outdoor conditions degraded similarly to samples submitted to controlled indoor tests, which suggest that the degradation mechanisms were similar, albeit on a different time scale.

As observed from the ISOS-L-1 standard indoor test, the NP-OSC device presented a longer T_{80} time than the ref-OSC device (14 days against 8 days). V_{oc} of both devices also remains relatively unchanged during the test. The drop of ref-OSC conversion efficiency follows the decrease in J_{sc} but is also influenced by FF instability. The fill factor of the NP-OSC device, on the other hand, remains unchanged during the entirety of the test and η tracks closely the behavior of J_{sc}. A possible explanation for the ref-OSC FF instability is the increase of exciton recombination rate associated by fullerene dimerization. This effect is not observed for the NP-OSC likely due to longer exciton lifetimes.

The NP-OSC device experienced a greater amount of IPCE losses due to outdoor exposure than the reference device, as can be verified in Fig. 11. Losses were concentrated on the 350–450 nm range (absorption by fullerene) which is a strong indication of the occurrence of dimerization. Losses also occurred on the 550–650 mn range most likely due to P3HT photodegradation. Despite the more severe relative losses, the NP-OSC device maintained a higher external quantum efficiency throughout the test as can bee seen in Fig. 12.

It is important to point out that the IPCE reduction of the NP-bearing device observed in Fig. 11 was more severe during the
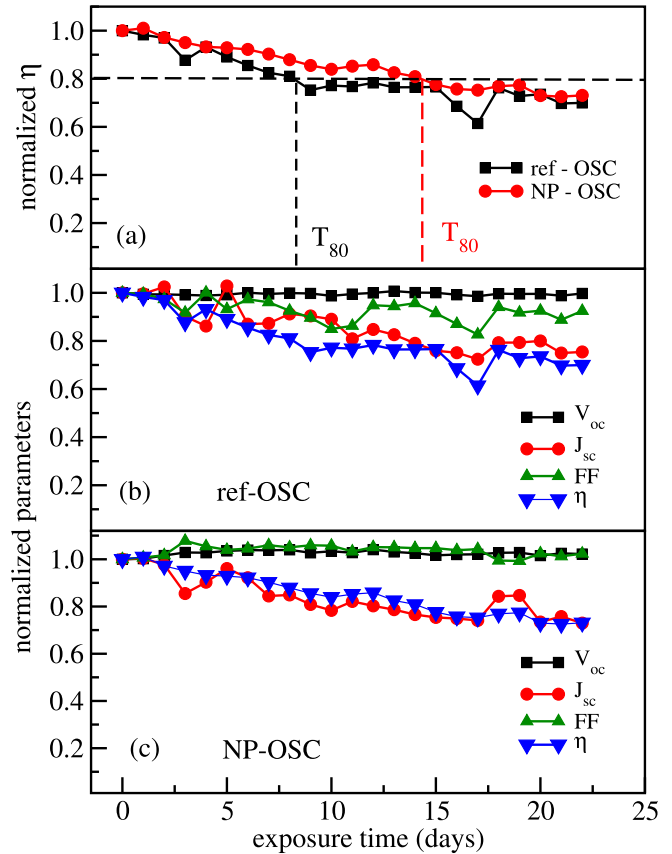
first 10 days as compared to the last 11 days of test. The reference device, on the other hand, experienced an almost linear decrease of IPCE. This result indicates that the presence of NP in the active layer led to faster degradation of the solar cell in the beginning of its lifetime, achieving stabilization before the reference device and maintaining a stronger IPCE after stabilization, which is desired in the long term.

4. Conclusion

Bulk heterojunction organic solar cells were built doping the P3HT:PCBM active layer with 10 at.% of Fe/SnO2 magnetic nanoparticles. Devices without NPs in the active layer were also produced to serve as reference. Slightly improved J_{sc}, together with a broader IPCE spectrum, suggests that addition of NPs to the devices contributed to the dissociation of photogenerated excitons into free charge carriers. Measurements of photocurrent density *vs.* effective bias voltage reinforces this suggestion. The increase of dissociated charge carriers is attributed to the presence of a week effective magnetic field in the active layer. This field increases the rate of intersystem crossing thus increasing the concentration of longer lived triplet excitons [6,7,14].

Stability studies following the ISOS-L-1 (indoors) and ISOS-O-2 (outdoors) protocols revealed an improved T_{80} for the NP-bearing devices. Degradation mechanisms were found to be likely the same for both reference and NP-doped cells, being mainly due to J_{sc} losses, which are closely related to PCBM dimerization. NP-OSCs experienced a strong initial drop in J_{sc} which was compensated by small improvements in V_{oc} and FF. It was shown that the
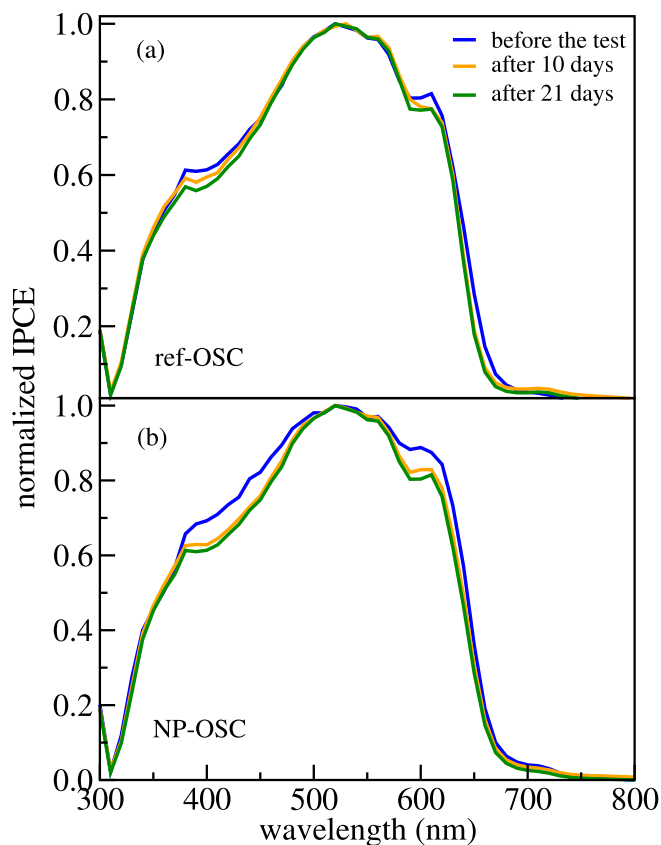
Fig. 11. ISOS-O-2 test: normalized IPCE measurements before the test, after 10 days of exposure and after 21 days of exposure (end of test) for (a) ref-OSC and (b) NP-OSC devices.
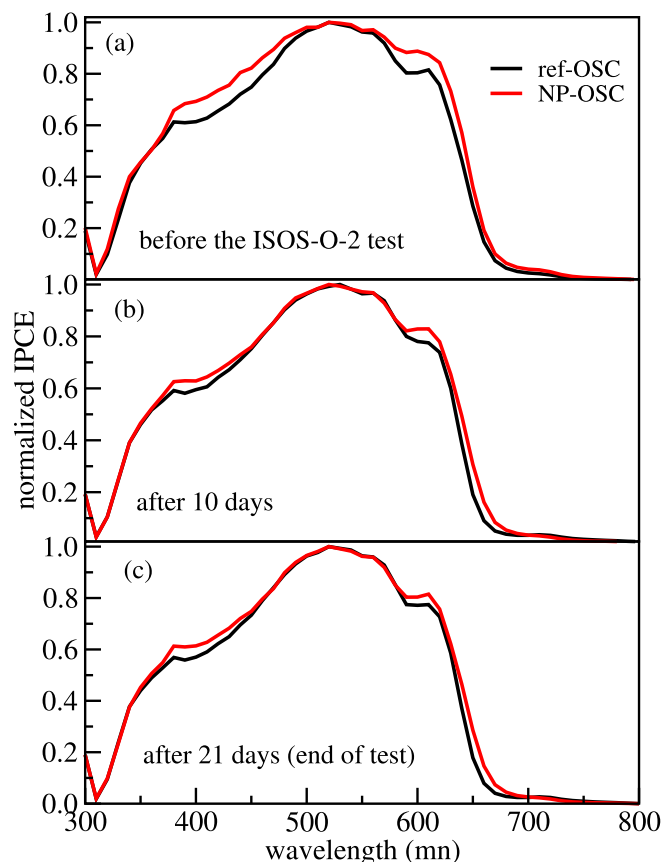

Fig. 12. ISOS-O-2 test: normalized IPCE normalized measurements for ref-OSC and NP-OSC devices (a) before the test, (b) after 10 days of exposure and (c) after 21 days of exposure (end of test).

presence of NPs in the active layer led to faster degradation of the solar cell in the beginning of its lifetime, nevertheless achieving stabilization before the reference device and maintaining a stronger IPCE after stabilization.

Doping of the active layer of OSCs with magnetic nanoparticles has been successfully used to modify the cells' electrical and optical properties. Improvements have been observed in aspects such as exciton dissociation and stability. The results obtained in this research work provide subsidies that propitiate an understanding of the effective action caused by the doping of the active layer of OSCs with magnetic NPs, thus opening new improvement opportunities by means of the addition of a degree of freedom for spin within the active layer. Using diluted magnetic semiconductor nanoparticles instead of ferromagnetic nanoparticles offers a new path of development for the field. The features shown by the NP-doped devices offer advantages in the long term and, therefore, the present work represents an evolution as it showed further evidence that addition of magnetic nanoparticles to bulk heterojunction organic solar cells is a promising path to enhanced power conversion efficiency and stability.

References

[1] T.R. Andersen, N.A. Cooling, F. Almyahi, A.S. Hart, N.C. Nicolaidis, K. Feron, M. Noori, B. Vaughan, M.J. Griffith, W.J. Belcher, P.C. Dastoor, Sol. Energy Mater. Sol. Cells 149 (2016) 103–109.
[2] D. Kaduwal, H.-F. Schleiermacher, J. Schulz-Gericke, S. Schiefer, Y.L. Tan, J. Zhang, B. Zimmermann, U. Würfel, Sol. Energy Mater. Sol. Cells 136 (2015) 200–205.
[3] F.C. Krebs, M. Hösel, M. Corazza, B. Roth, M.V. Madsen, S.A. Gevorgyan, R.R. Søndergaard, D. Karg, M. Jørgensen, Energy Technol. 1 (2013) 378–381.
[4] J. Huang, J.H. Carpenter, C.-Z. Li, J.-S. Yu, H. Ade, A.K.Y. Jen, Adv. Mater 28 (2016) 967.
[5] X. Gong, Y. Jiang, C. Zhang, L. Yang, M. Li, H. Ma, Appl. Phys. A 122 (2016) 287.
[6] K. Wang, C.Y.C. Liu, X. Hu, S. Chuan, X. Gong, Sci. Rep. 5 (2015) 9265.
[7] K. Wang, H. Ren, C. Yi, C. Liu, H. Wang, L. Huang, H. Zhang, A. Karim, X. Gong, ACS Appl. Mater. Interfaces 5 (2013) 10325–10330.
[8] G. Téran-Escobar, J. Pampel, J.M. Caicedo, M. Lira-Cantú, Energy Environ. Sci. 6 (2013) 3088.
[9] M.D. Irwin, D.B. Buchholz, A.W. Hains, R.P.H. Chang, T.J. Marks, PNAS 105 (2008) 2783–2787.
[10] W.A. Hammed, R. Yahya, A.L. Bola, H.N.M.E. Mahmud, Energies 6 (2013) 5847–5868.
[11] Y.S. Kim, Y. Lee, J.K. Kim, E.O. Seo, E.W. Lee, W. Lee, S.H. Han, S.H. Lee, Curr. Appl. Phys. 10 (2010) 985–989.
[12] M. Dante, J. Peet, T.-Q. Nguyen, J. Phys. Chem. C 112 (2008) 7241–7249.
[13] F.C. Chen, C.J. Ko, J.L. Wu, W.C. Chen, Sol. Energy Mater. Sol. Cells 94 (2010) 2426–2430.
[14] E.-P. Yao, Y.-J. Tsai, W.-C. Hsu, Phys. Chem. Chem. Phys. 17 (2015) 5826.
[15] O.V. Mikhnenko, R. Ruiter, P.W.M. Blom, M.A. Loi, Phys. Rev. Lett. 108 (2012) 137401.
[16] M. Samiullah, D. Moghe, U. Scherf, S. Guha, Phys. Rev. B 82 (2010) 205211.
[17] S.R. Scully, M.D. McGehee, J. Appl. Phys. 100 (2006) 34907.
[18] Y. Kim, D. Bradley, Curr. Appl. Phys. 5 (2005) 222–226.

[19] B. Xu, S. Holdcrofl, Thin Solid Films 242 (1994) 174.
[20] A.E. Cohen, J. Phys. Chem. A 113 (2009) 11084–11092.
[21] C.J. Sun, Y. Wu, Z. Xu, B. Hu, J. Bai, J.P. Wang, J. Shen, Appl. Phys. Lett. 90 (2007) 232110.
[22] D.M. González, V. Körstgens, Y. Yao, L. Song, G. Santoro, S.V. Roth, P. Müller-Buschbaum, Adv. Energy Mater 5 (2015) 1401770.
[23] W. Zhang, Y. Xu, H. Wang, C. Xu, S. Yang, Sol. Energy Mater. Sol. Cells 95 (2011) 2880.
[24] C.J. Mulligan, C. Bilen, X. Zhou, W.J. Belcher, P.C. Dastoor, Sol. Energy Mater. Sol. Cells 133 (2015) 26.
[25] A. Gambhir, P. Sandwell, J. Nelson, Sol. Energy Mater. Sol. Cells 156 (2016) 49–58.
[26] P. Cheng, X. Zhan, Chem. Soc. Rev. 9 (2016) 2544–2582.
[27] A.M. Nardes, M. Kemerink, M.M. de Kok, E. Vinken, K. Maturova, R.A.J. Janssen, Org. Electron 9 (2008) 727.
[28] T.S. Glen, N.W. Scarratt, H. Yi, A. Iraqi, T. Wang, J. Kingsley, A.R. Buckley, D.G. Lidzey, A.M. Donald, Sol. Energy Mater. Sol. Cells 140 (2015) 25.
[29] W.J. Yu, L. Shen, S.P. Ruan, F.X. Meng, J.L. Wang, E.R. Zhang, W.Y. Chen, Sol. Energy Mater. Sol. Cells 98 (2012) 212.
[30] J. Jung, D. Kim, W.S. Shin, S.J. Moon, C. Lee, S.C. Yoon, Jpn. J. Appl. Phys. 49 (5) (2010) 05EB05.
[31] A.K.K. Kyaw, X.W. Sun, C.Y. Jiang, G.Q. Lo, D.W. Zhao, D.L. Kwong, Appl. Phys. Lett. 93 (2008) 221107.
[32] S. Han, W.S. Shin, M. Seo, D. Gupta, S.J. Moon, S. Yoo, Org. Electron 10 (2009) 791.
[33] A. Morais, J.P.C. Alves, F.A.S. Lima, M. Lira-Cantu, A.F. Nogueira, J. Photonics Energy 5 (2015) 057408.
[34] F.A.S. Lima, M.J. Beliatis, B. Roth, T.R. Andersen, A. Bortoti, Y. Reyna, E. Castro, I.F. Vasconcelos, S.A. Gevorgyan, F.C. Krebs, M. Lira-Cantu, APL Mater 4 (2016) 026104.
[35] K. Zilberberg, S. Trost, J. Meyer, A. Kahn, A. Behrendt, D. Lützenkirchen-Hecht, R. Frahm, T. Riedl, Adv. Func. Mater 21 (2011) 4776.
[36] B.H. Toby, J. Appl. Cryst. 34 (2001) 210.
[37] C.E.R. Torres, A.F. Cabrera, F.S. Sanchez, Phys. B 389 (2007) 176.
[38] D.H. Wang, D.-G. Choi, O.O. Park, J.H. Park, J. Mater. Chem. 20 (2010) 4910–4915.
[39] J.C. Blakesley, D. Neher, Phys. Rev. B 84 (2011) 075210.
[40] N.K. Elumalai, A. Uddin, Energy Environ. Sci. 9 (2016) 391.
[41] D. Bartesaghi, I.C. Prez, J. Kniepert, S. Roland, M. Turbiez, D. Neher, L.J.A. Koster, Nat. Commun. 6 (2015) 7083.
[42] C. Schwarz, S. Tscheuschner, J. Frisch, S. Winkler, N. Koch, H. Bässler, A. Köhler, Phys. Rev. B 87 (2013) 155205.
[43] Y. Yao, X. Xie, H. Ma, J. Phys. Chem. Lett. 7 (2016) 4830–4835.
[44] S. Few, J.M. Frostab, J. Nelson, Phys. Chem. Chem. Phys. 17 (2015) 2311–2325.
[45] G. D'Avino, L. Muccioli, Y. Olivier, D. Beljonne, J. Phys. Chem. Lett. 7 (2016) 536–540.
[46] R.A. Street, Adv. Mater 28 (2016) 3814–3830.
[47] V.I. Arkhipov, E.V. Emelianova, H. Bässler, Chem. Phys. Lett. 372 (2003) 886–892.
[48] V.I. Arkhipov, P. Heremans, H. Bässler, Appl. Phys. Lett. 82 (2003) 4604–4607.
[49] S. Dag, L.-W. Wang, J. Phys. Chem. B 144 (2010) 5997–6000.
[50] A. Miglio, R. Saniz, D. Waroquiers, M. Stankovski, M. Giantomassi, G. Hautier, G.-M. Rignanese, X. Gonze, Opt. Mater. 38 (2014) 161–166.

[51] M. Dou, C. Persson, J. Appl. Phys. 113 (2013) 083703.
[52] A. Rivaton, S. Chambon, M. Manceau, J. Gardette, N. Lemaître, S. Guillerez, Polym. Degrad. Stab. 95 (2010) 278–284.
[53] B.H. Johnson, E. Allagoa, R.L. Thomas, G. Stettler, M. Wallis, J.H. Peel, T. Adalsteinsson, B.J. McNelis, R.P. Barber Jr., Sol. Energy Mater. Sol. Cells 94 (2009) 537–541.
[54] R. de Bettignies, F. Leroy, M. Firon, C. Sentein, Synth. Met. 156 (2006) 510–513.
[55] S. Bertho, G. Janssen, T.J. Clei, B. Conings, W. Moons, A. Gadisa, J.D. Haen, E. Goovaerts, L. Lutsen, J. Manca, D. Vanderzande, Sol. Energy Mater. Sol. Cells 92 (2008) 753–760.
[56] K. Kawano, R. Pacios, D. Poplavskyy, J. Nelson, D.D.C. Bradley, J.R. Durrant, Sol. Energy Mater. Sol. Cells 90 (2006) 3520–3530.
[57] A. Seemann, T. Sauermann, C. Lungenschmied, O. Armbruster, S. Bauer, H.-J. Egelhaaf, J. Hauch, Sol. Energy 85 (2011) 1238–1249.
[58] M.O. Reese, S.A. Gevorgyan, M. Jorgensen, E. Bundgaard, S.R. Kurtz, D.S. Ginley, D.C. Olson, M.T. Lloyd, P. Morvillo, E.A. Katz, A. Elschner, O. Haillant, T.R. Currier, V. Shrotriya, M. Hermenau, M. Riede, K.R. Kirov, G. Trimmel, T. Rath, O. Inganas, F. Zhang, M. Andersson, K. Tvingstedt, M. Lira-Cantú, D. Laird, C. McGuiness, S. Gowrisanker, M. Pannone, M. Xiao, J. Hauch, R. Steim, D.M. DeLongchamp, R. Rosch, H. Hoppe, N. Espinosa, A. Urbina, G. Yaman-Uzunoglu, J. Bonekamp, A.J.J.M. van Breemen, C. Girottou, E. Voroshazi, F.C. Krebs, Sol. Energy Mater. Sol. Cells 95 (2011) 1253–1267.
[59] C.H. Peters, I.T. Sachs-Quintana, W.R. Mateker, T. Heumueller, J. Rivnay, R. Noriega, Z.M. Beiley, E.T. Hoke, A. Salleo, M.D. McGehee, Adv. Mater 24 (2012) 663–668.
[60] R. Pacios, A.J. Chatten, K. Kawano, J.R. Durrant, D.D.C. Bradley, J. Nelson, Adv. Func. Mater 16 (2006) 2117–2126.
[61] L. Córcolesa, J. Abad, J. Padilla, A. Urbina, Sol. Energy Mater. Sol. Cells 141 (2015) 423–428.
[62] P. Kumar, C. Bilen, B. Vaughan, X. Zhou, P.C. Dastoor, W.J. Belcher, Sol. Energy Mater. Sol. Cells 149 (2016) 179–186.
[63] T. Heumueller, W.R. Mateker, A. Distler, U.F. Fritze, R. Cheacharoen, W.H. Nguyen, M. Biele, M. Salvador, M. von Delius, H. Egelhaaf, M.D. McGehee, C.J. Brabec, Energy Environ. Sci. 9 (2016) 247–256.
[64] N. Grossiord, J.M. Kroon, R. Andriessen, P.W.M. Blom, Org. Electron 13 (2012) 432–456.
[65] R.A. Street, J.E. Northrup, B.S. Krusor, Phys. Rev. B 85 (2012) 205211.
[66] J. Bhattacharya, R.W. Maye, M. Samiee, V.L. Dalal, Appl. Phys. Lett. 100 (2012) 193501.
[67] A. Distler, T. Sauermann, H. Egelhaaf, S. Rodman, D. Waller, K. Cheon, M. Lee, D.M. Guldi, Adv. Energy Mater 4 (2013) 1300693.
[68] T.M. Clarke, C. Lungenschmied, J. Peet, N. Drolet, K. Sunahara, A. Furube, J.A. Mozer, Adv. Energy Mater 3 (2013) 1473–1483.
[69] N. Wang, X. Tong, Q. Burlingame, J. Yu, S.R. Forrest, Sol. Energy Mater. Sol. Cells 125 (2014) 170–175.
[70] Q. Burlingame, X. Tong, J. Hankett, M. Slootsky, Z. Chen, S.R. Forrest, Energy Environ. Sci. 8 (2015) 1005–1010.
[71] S. Trost, K. Zilberberg, A. Behrendt, A. Polywka, P. Gorrn, P. Reckers, J. Maibach, T. Mayer, T. Riedl, Adv. Energy Mater (2013) 201300402.
[72] A. Sundqvist, O.J. Sandberg, M. Nyman, J. Smatt, R. Osterbacka, Adv. Energy Mater 6 (2016) 1502265.